Influence of four-phonon scattering and wavelike phonon tunneling effects on the thermal transport properties of $TlBiSe_2$

Linxuan Ji,[1] Anqi Huang,[1] Yiqi Huo,[1] Yi-min Ding,[2] Shuming Zeng,[3] Yu Wu,[2,*] and Liujiang Zhou[1,2,†]

[1]*School of Physics, State Key Laboratory of Electronic Thin Films and Integrated Devices, University of Electronic Science and Technology of China, Chengdu 611731, China*

[2]*Yangtze Delta Region Institute (Huzhou), University of Electronic Science and Technology of China, Huzhou 313001, China*

[3]*College of Physics Science and Technology, Yangzhou University, Jiangsu 225009, China*

(Received 2 April 2024; revised 14 May 2024; accepted 4 June 2024; published 18 June 2024)

$TlBiSe_2$ is considered a potential thermoelectric material due to its ultralow lattice thermal conductivity κ_L and excellent electrical properties. However, previous studies on the thermal properties of $TlBiSe_2$ only considered the effects of three-phonon scattering, which resulted in significant differences between theoretical and experimental values. In this material, four-phonon scattering processes mainly reduce the thermal transport of acoustic phonons, resulting in an approximate 28% reduction in particlelike thermal conductivity κ_p at 300 K. The high-frequency optical branches are dense and the phonon lifetime is short, making it easy to generate wavelike phonon tunneling. After considering wavelike thermal conductivity κ_c, κ_L along the in-plane direction is in good agreement with the experimental values. A nonstandard $\kappa_L \propto T^{-0.36}$ dependence is revealed in the cross-plane direction. At high temperatures, κ_c in the cross-plane direction is greater than κ_p and κ_c dominates the thermal transport with 61% of κ_L at 700 K. In addition to the frequency difference of the phonon pairs, the interbranch phonon group velocity also has an important effect on κ_c. Our work improves the calculational accuracy of thermal conductivity for $TlBiSe_2$ and broadens the field for application of ternary-layered thallium-based semiconductors.

DOI: 10.1103/PhysRevB.109.214307

I. INTRODUCTION

The increasing global energy scarcity and environmental issues have resulted in numerous social and political problems [1]. The utilization of nonrenewable energy sources such as fossil fuels not only leads to environmental pollution but also exhibits low efficiency, with approximately 60% of the generated energy being released as waste heat [2]. In the past few years, thermoelectric (TE) materials have garnered significant attention due to their ability to directly and reversibly convert thermal and electrical gradients, providing an effective means for sustainable development [3]. The performance of TE materials is quantified by a dimensionless figure of merit known as $ZT = S^2\sigma T/\kappa_{\text{total}}$, where S is the Seebeck coefficient, σ is the electrical conductivity, κ_{total} is the total thermal conductivity including both electronic (κ_e) and lattice (κ_L) contributions, and T is the absolute temperature [4]. Due to the strong coupling between S, σ, and κ_e, it is hard to regulate these parameters independently. Fortunately, as a relatively independent parameter, κ_L is weakly coupled to the above parameters. Thus, finding materials with intrinsically low κ_L is an effective way and the main challenge to increase ZT.

In recent years, topological insulators have been considered as potential excellent TE materials due to their intrinsically low κ_L [5,6]. Many currently known topological insulators share common properties such as heavy atoms, large orbital-spin coupling, and narrowband gaps [7–9]. $TlBiSe_2$ is an important topological insulator with a chalcopyrite structure. As a ternary-layered thallium-based semiconductor compound, it has garnered significant attention for its electrical and thermal transport properties [10,11]. On the one hand, the presence of Tl ions connecting the layers in $TlBiSe_2$, as opposed to Bi_2Se_3, leads to stronger covalent bonding [12]. This will have a significant impact on the electrical performance of the material. By solving the Wiedemann-Franz law, KaniAmuthan *et al.* [13] obtained a power factor of $2.956\,\mu W\,m^{-1}\,K^{-2}$ for $TlBiSe_2$. On the other hand, $TlBiSe_2$ has a band gap of 0.347 eV and there are $6s^2$ dual-cation lone pair electrons as well as metavalent bonding in its structure, which result in strong anharmonicity [10]. Ding *et al.* [14] solved the phonon Boltzmann transport equation (PBTE) to calculate the κ_L of $TlBiSe_2$ with $0.85\,W\,m^{-1}\,K^{-1}$ at 300 K in the in-plane direction. Recently, Maria *et al.* [15] synthesized high-quality samples of $TlBiSe_2$ and experimentally measured its thermoelectric performance. The κ_L measured by the experiment is $1.16\,W\,m^{-1}\,K^{-1}$ at 300 K, which further decreases to $0.48\,W\,m^{-1}\,K^{-1}$ at 720 K. Previous research has indeed indicated that $TlBiSe_2$ is a highly promising thermoelectric material. However, the calculated κ_L shows a significant deviation of approximately $0.31\,W\,m^{-1}\,K^{-1}$ from the experimental value. Therefore, improving the calculation method to obtain more accurate thermoelectric transport parameters is the main challenge to enhance $TlBiSe_2$ performance.

In relevant thermal properties studies of $TlBiSe_2$, calculations are often focused on three-phonon (3ph) scattering while

*Contact author: wuyu9573@qq.com
†Contact author: ljzhou@uestc.edu.cn

neglecting the influence of high-order 4ph scattering on κ_L [16]. This omission will lead to a large discrepancy between the calculated value and the actual measurements, particularly in materials with characteristics such as large acoustic-optical band gap, acoustic bunching, and the flatness of the optical bands [17]. Moreover, a single form of phonon may not be sufficient to fully describe the thermal transport properties in complex structures. In fact, the wave-particle duality of phonons is not unique to nanomaterials but also applies to bulk crystals [18]. When there are dense spectral lines in the phonon dispersion, the contribution of wavelike thermal conductivity κ_c to thermal transport will be more obvious [19].

In this work, we systematically study the lattice thermal transport properties of $TlBiSe_2$ from the perspective of the 4ph interactions and wavelike phonon tunneling effect by first-principles calculations. After considering 4ph scattering, we find that the calculated particlelike thermal conductivity κ_p is 28% lower than that found considering only 3ph scattering. Further phonon scattering analysis shows that 4ph scattering mainly increases the scattering rate of acoustic phonons and thus results in the significant decrease of κ_p. In addition, the calculated κ_c shows that the wavelike phonon tunneling effect in this material is particularly obvious. The κ_c is obtained by calculating the off-diagonal terms of the Wigner heat-flux operator. In the cross-plane direction, κ_c dominates the thermal transport with 61% of κ_L at 700 K. Due to the large interbranch phonon group velocity, phonon pairs with larger frequency differences also contribute significantly to κ_c. Finally, the κ_L obtained by adding κ_p and κ_c is in good agreement with the experimental value. This work reveals the microscopic mechanism of phonon thermal transport in $TlBiSe_2$, which provides an important idea for the future study of thermal properties of ternary-layered thallium-based semiconductors.

II. COMPUTATIONAL METHODS

In this work, all the density functional theory calculations [20] are done using the plane-wave projector augmented-wave pseudopotentials [21] and Perdew-Burke-Ernzerhof exchange-correlation functionals [22] as implemented in the Vienna *ab initio* simulation package (VASP) [23]. Our first step is to optimize the structure of $TlBiSe_2$. We use $14 \times 14 \times 14$ Monkhorst-Pack k-point grids to sample the Brillouin zone (BZ). In this structure relaxation process, the plane-wave energy cutoff is chosen as 450 eV. The energy convergence criterion for optimizing atomic positions is set to 10^{-5} eV between two consecutive steps, while the maximum Hellmann-Feynman force convergence threshold is defined as 10^{-3} eV Å^{-1} for each atom.

To obtain an accurate κ_L, the harmonic and anharmonic interatomic force constants (IFCs), namely, the second-, third-, and fourth-order IFCs, need to be calculated precisely and used as inputs to solve the PBTE [24]. We employ the temperature-dependent effective potential (TDEP) [25] to fit second- and third-order IFCs at the finite temperature using the *ab initio* molecular dynamics (AIMD) simulation results for $TlBiSe_2$ crystal. The recently introduced on-the-fly machine learning potential of VASP is used to accelerate the AIMD simulation. The AIMD simulation employs a $4 \times 4 \times 4$ supercell comprising 256 atoms, utilizing the Γ point for Brillouin-zone integration and employing a convergence threshold of 10^{-5} eV for the electronic self-consistent-field iterations. The simulation trajectories are 20 ps in duration, with a time step of 1 fs. The results show that AIMD has reached equilibrium (see the Supplemental Material [26]). The cutoff radius is set to 5 Å for both the third- and fourth-order IFCs.

By utilizing the IFCs obtained as mentioned above, the κ_L can be calculated by iteratively solving the PBTE for the nonequilibrium distribution function. This procedure is implemented in the SHENGBTE and FOURPHONON packages [27,28]. The code used to calculate κ_c has been integrated into SHENGBTE software by us [29]. According to the Wigner transport equation as derived from the Wigner phase-space formulation of quantum mechanics [30,31], the lattice thermal conductivity $\kappa_L^{\alpha\beta}$ can be expressed as the addition of particle-like ($\kappa_p^{\alpha\beta}$) and glasslike ($\kappa_c^{\alpha\beta}$) coherence

$$\kappa_L^{\alpha\beta} = \kappa_p^{\alpha\beta} + \kappa_c^{\alpha\beta}, \tag{1}$$

where α and β index the Cartesian directions. The populations' thermal conductivity is contributed by the particlelike phonons and can be obtained from the diagonal ($s = s'$) term of the Wigner heat-flux operator, which is calculated in the same way as the Peierls-Boltzmann thermal conductivity results; thus it is expressed as

$$\kappa_p^{\alpha\beta} = \frac{1}{VN_{\mathbf{q}}} \sum_{\mathbf{q}s} C_{\mathbf{q}}^s v_{\mathbf{q},\alpha}^s v_{\mathbf{q},\beta}^s \tau_{\mathbf{q}}^s. \tag{2}$$

The thermal conductivity of the coherence is from off-diagonal ($s \neq s'$) terms, which describes the tunneling effect between different phonon branches s and s',

$$\kappa_c^{\alpha\beta} = \frac{\hbar^2}{k_B T^2 V N_{\mathbf{q}}} \sum_{\mathbf{q}} \sum_{s \neq s'} \frac{\omega_{\mathbf{q}}^s + \omega_{\mathbf{q}}^{s'}}{2} v_{\mathbf{q},\alpha}^{s,s'} v_{\mathbf{q},\beta}^{s,s'} \times \frac{\omega_{\mathbf{q}}^s n_{\mathbf{q}}^s \left(n_{\mathbf{q}}^s + 1\right) + \omega_{\mathbf{q}}^{s'} n_{\mathbf{q}}^{s'} \left(n_{\mathbf{q}}^{s'} + 1\right)}{4\left(\omega_{\mathbf{q}}^s - \omega_{\mathbf{q}}^{s'}\right)^2 + \left(\Gamma_{\mathbf{q}}^s + \Gamma_{\mathbf{q}}^{s'}\right)^2} \left(\Gamma_{\mathbf{q}}^s + \Gamma_{\mathbf{q}}^{s'}\right), \tag{3}$$

where $\hbar$ denotes the reduced Plank constant, k_B denotes the Boltzmann constant, V denotes the volume of the unit cell, and $N_{\mathbf{q}}$ denotes the number of sampled phonon wave vectors in the first Brillouin zone. In addition, $C_{\mathbf{q}}^s$, $v_{\mathbf{q}}^s$, $\tau_{\mathbf{q}}^s$, $\omega_{\mathbf{q}}^s$, $v_{\mathbf{q}}^{s,s'}$, and $\Gamma_{\mathbf{q}}^s$ ($\tau_{\mathbf{q}}^s = 1/\Gamma_{\mathbf{q}}^s$) are the heat capacity, the group velocity, the lifetime, the phonon frequency, the interbranch phonon group velocity, and the scattering rate of a phonon mode, respectively; $n_{\mathbf{q}}^s = [\exp(\hbar\omega_{\mathbf{q}}^s / k_B T) - 1]^{-1}$ represents the equilibrium Bose-Einstein distribution.

III. RESULTS AND DISCUSSION

A. Crystal structure and phonon dispersion

$TlBiSe_2$ has a rhombohedral primitive cell as well as a conventional hexagonal cell and its space group $D_{3d}^5(R\bar{3}m)$ is the same as for the topological insulator Bi_2Se_3. Although both of them have the same space group, the atomic layers are stacked differently. In Fig. 1(a), Bi_2Se_3 consists of five-atom layers, stacked in the c direction with a sequence of -Bi-Se-Bi-Se-Bi-, which are connected by weak van der Waals

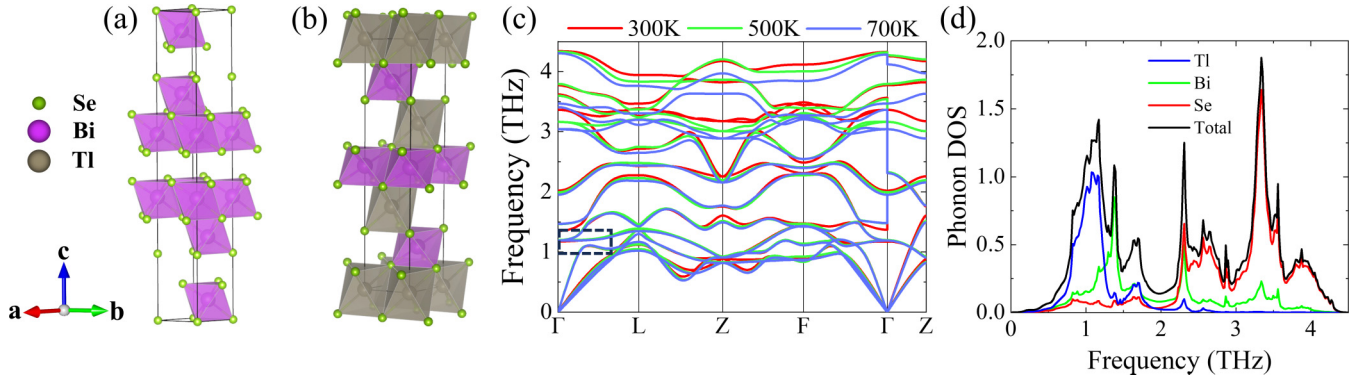

FIG. 1. Comparison of the conventional hexagonal cell of (a) Bi_2Se_3 and (b) $TlBiSe_2$. The brown and purple octahedra represent the TlS_6 and BiS_6 geometries, respectively. (c) Calculated phonon dispersion relations along high symmetry directions at different temperatures. The black dotted box indicates the phenomenon of avoided crossing. (d) Atom-projected phonon density of states (DOS) at 300 K for $TlBiSe_2$.

interactions between different layers [32]. In Fig. 1(b), because of the Tl atoms within the layers, $TlBiSe_2$ has atomic layers stacked in the sequence -Se-Tl-Se-Bi-Se-, which gives rise to stronger covalent bonding [12] compared with Bi_2Se_3. The relaxation lattice parameters are $a = b = 4.28$ Å and $c = 22.75$ Å for the conventional hexagonal cell, which agree well with the previous results [33].

An electron localization function (ELF) equal to 0 corresponds to no localization, an ELF equal to 0.5 represents delocalized electron gas, and an ELF equal to 1 indicates complete localization. The ELF between Bi and Se atoms reaches approximately 0.35, indicating that it is predominantly connected by covalent bonds (see the Supplemental Material [26]). The temperature-dependent phonon dispersion with LO-TO splitting for three different temperatures is displayed in Fig. 1(c). There are three acoustic and nine optical phonon branches corresponding to the four atoms per primitive cell. The phonon modes have no imaginary frequencies, indicating the dynamic stability of $TlBiSe_2$. It is clear that the acoustic frequencies do not change notably, but the optical frequencies show softening with increasing temperature. The maximum frequency of acoustic phonon modes for $TlBiSe_2$ is 1.39 THz at 500 K, which is close to 1.5 THz for Bi_2Te_3 [34]. The black dashed box in Fig. 1(c) indicates that there is an avoided crossing behavior between the acoustic branches and the low-frequency optical branches. This makes the acoustic branches flatter, causing a reduction in group velocity in the avoidance region [35]. The corresponding atom-projected phonon density of states (DOS) at 300 K is shown in Fig. 1(d). It can be seen that the acoustic modes are dominated by the Tl atoms. In contrast, the low- and high-frequency optical modes are contributed by the Bi and Se atoms, respectively. It is worth noting that the vibration of the Se atom contributes throughout most of the frequency range, indicating the formation of delocalized bonding between the Se and Bi atoms [36]. Tl atoms act as rattling atoms in $TlBiSe_2$ [37]; thus the corresponding phonon DOS value is localized between 0.5 and 1.5 THz.

In this material, the long-range interaction (LRI) will cause optical phonon softening, strong anharmonic scattering, and large phase space [38]. We show the phonon spectra under different cutoff radii in the Supplemental Material [26]. The bond length of Se-Se pairs in Se-Bi-Se is 5.97 Å and the cutoff radii of 5.85 and 6.00 Å were set when extracting the second-order IFCs. This preserves the LRI of Se-Se pairs in Se-Bi-Se when the cutoff radius is set to 6.00 Å and the LRI is eliminated when it is set to 5.85 Å. The low-frequency optical phonon modes are hardened when reducing the cutoff radius. Similarly, the influence of the LRI of Se-Se pairs in Se-Tl-Se on the phonon dispersion is studied. The length of Se-Se pairs in Se-Tl-Se is approximately 6.61 Å. Compared with Se-Se pairs in Se-Bi-Se, the phonon dispersion does not change significantly after removing the LRI in Se-Tl-Se.

B. Four-phonon scattering processes

It can be seen from the phonon dispersion that 3ph scattering channels in $TlBiSe_2$ will be suppressed, which will make 4ph scattering more obvious [16]. The acoustic phonon modes are mainly contributed by Tl rattling atoms, which exhibit dense and flat features. Hence, the three-acoustic-phonon (*aaa*) interactions [39] are suppressed, which further limits 3ph scattering channels. This is analogous to a straightforward argument that three phonons from the same acoustic branch cannot simultaneously satisfy both momentum and energy conservation [40]. The IFC of the nearest Tl-Se atomic pairs is 0.31 eV/Å^2, while the IFC of the nearest Bi-Se atomic pairs is 1.56 eV/Å^2, indicating a stronger interaction between Bi and Se compared to Tl and Se. The contribution of Se atoms to a wide range of phonon spectra will lead to lattice softening and enhance the anharmonicity of this material [36]. Additionally, the phonon dispersions of $TlBiSe_2$ prominently exhibit flat optical branches, which significantly weaken the three-optical-phonon (*ooo*) interactions due to the energy-conservation rule. Because *aaa* and *ooo* scattering are inhibited, the proportion of the acoustic-acoustic-optical (*aao*) interactions and the acoustic-optical-optical (*aoo*) interactions is likely to increase. Furthermore, the flatness of the optical bands reflects that $TlBiSe_2$ has relatively small group velocities for its optical modes, which is consistent with the group velocities of phonons (see the Supplemental Material [26]). The acoustic branches have large negative γ values, which is caused by the enhanced independent atomic vibration of Tl rattling atoms (see the Supplemental Material [26]). These rattling modes are found to be highly anharmonic, which results in low κ_L [41].

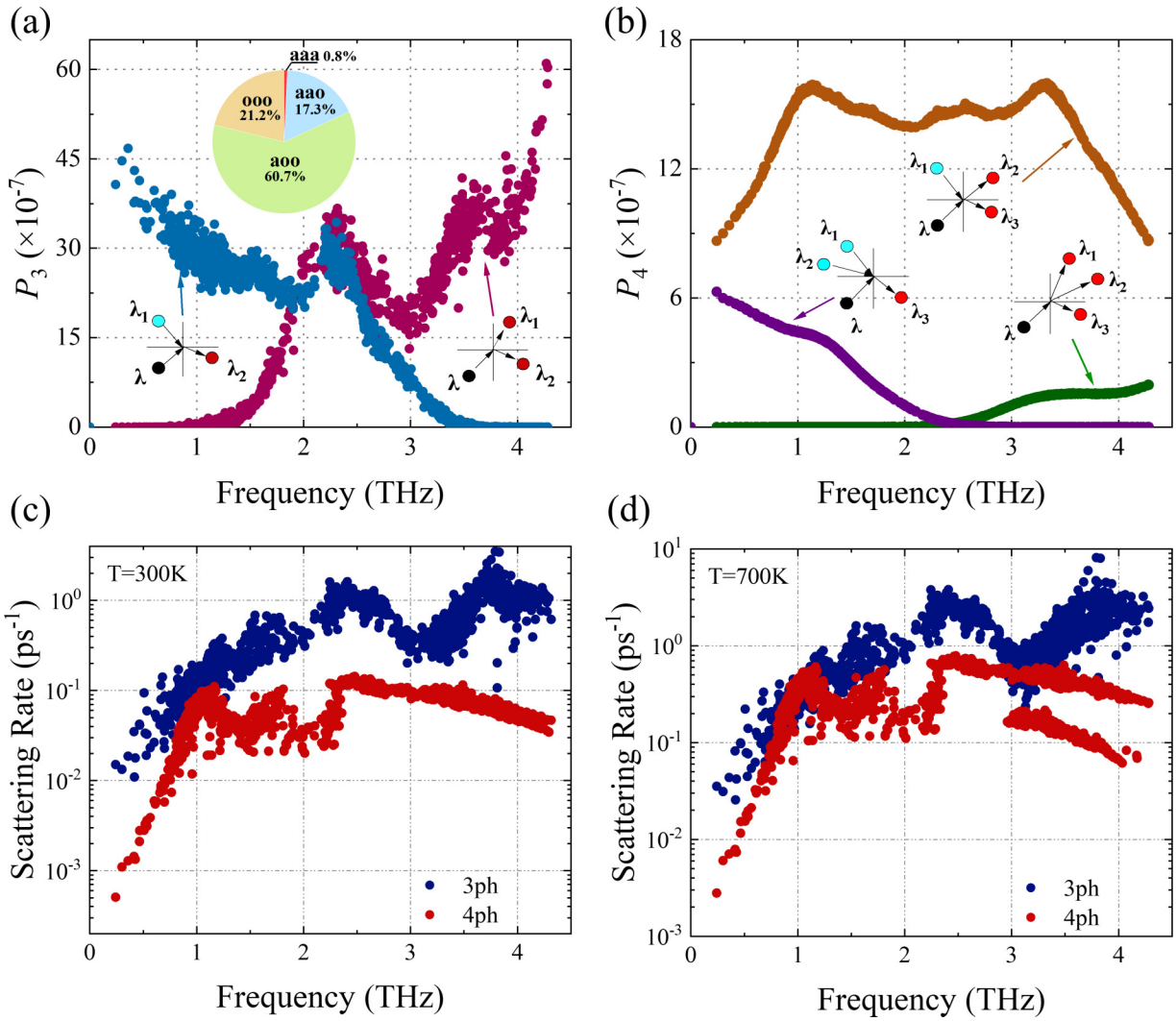

FIG. 2. Calculated phase space for (a) 3ph and (b) 4ph scattering at 300 K decomposed into the absorption ($\lambda + \lambda_1 \rightarrow \lambda_2$), emission ($\lambda \rightarrow \lambda_1 + \lambda_2$), combination ($\lambda + \lambda_1 + \lambda_2 \rightarrow \lambda_3$), redistribution ($\lambda + \lambda_1 \rightarrow \lambda_2 + \lambda_3$), and splitting ($\lambda \rightarrow \lambda_1 + \lambda_2 + \lambda_3$) processes, which are represented by blue, red, purple, brown, and green scatters, respectively. The inset in (a) shows the proportion of *aaa*, *aao*, *aoo*, and *ooo* in phase space for 3ph scattering. Calculated intrinsic 3ph scattering rate (blue circles) and 4ph scattering rate (red circles) as a function of frequency for $TlBiSe_2$ at (c) 300 K and (d) 700 K, respectively.

To further investigate phonon scattering mechanisms, the phonon phase space is calculated and shown in Fig. 2. Figure 2(a) displays the phase-space decomposition diagram for 3ph scattering processes as a function of frequency. The blue scatters represent the absorption process ($\lambda + \lambda_1 \rightarrow \lambda_2$) and the red scatters represent the emission process ($\lambda \rightarrow \lambda_1 + \lambda_2$). In the low-frequency range, scattering processes mainly involve the merging of two lower-energy phonons into one higher-energy phonon. With increased frequency, phonons are more prone to split into two lower-frequency phonons. The inset of Fig. 2(a) shows the decomposed 3ph scattering channels. It can be seen that *aoo* scattering is dominant in 3ph scattering processes with 60.7%, while *aaa* scattering channels are suppressed with only 0.8%. Also, the corresponding phase-space decomposition diagram for the 4ph scattering processes is shown in Fig. 2(b). The 4ph scattering processes can occur in three different forms, combination ($\lambda + \lambda_1 + \lambda_2 \rightarrow \lambda_3$), redistribution ($\lambda + \lambda_1 \rightarrow \lambda_2 + \lambda_3$), and splitting ($\lambda \rightarrow \lambda_1 + \lambda_2 + \lambda_3$), which are represented by purple, brown, and green scatters, respectively. The redistribution processes play a dominant role in 4ph scattering processes because the energy conservation for the 4ph interactions is more easily satisfied in this process.

In contrast to the well-studied behavior of classical 3ph scattering processes, 4ph scattering processes in bulk $TlBiSe_2$ have not been investigated previously. As shown in Fig. 3(a), we calculated κ_p of $TlBiSe_2$ in the in-plane (*a*-axis) and cross-plane (*c*-axis) directions considering 3ph and (3 + 4)ph scattering. Because different layers in Bi_2Se_3 are coupled by weak van der Waals interactions, the thermal anisotropy is very obvious, with a significant difference in κ_p between the in-plane and cross-plane directions [42]. The ratio of in-plane κ_p to cross-plane κ_p is 3.5 in Bi_2Se_3. However, due to the presence of Tl atoms connecting the $TlBiSe_2$ layers, the difference of κ_p along the *a* and *c* axes decreases significantly, resulting in a ratio of 1.15. Considering 3ph scattering, the calculated κ_p is 1.44 and 1.49 $W\,m^{-1}\,K^{-1}$ at 300 K along the *a* and *c* axes, respectively. Taking 4ph scattering into account in cal-

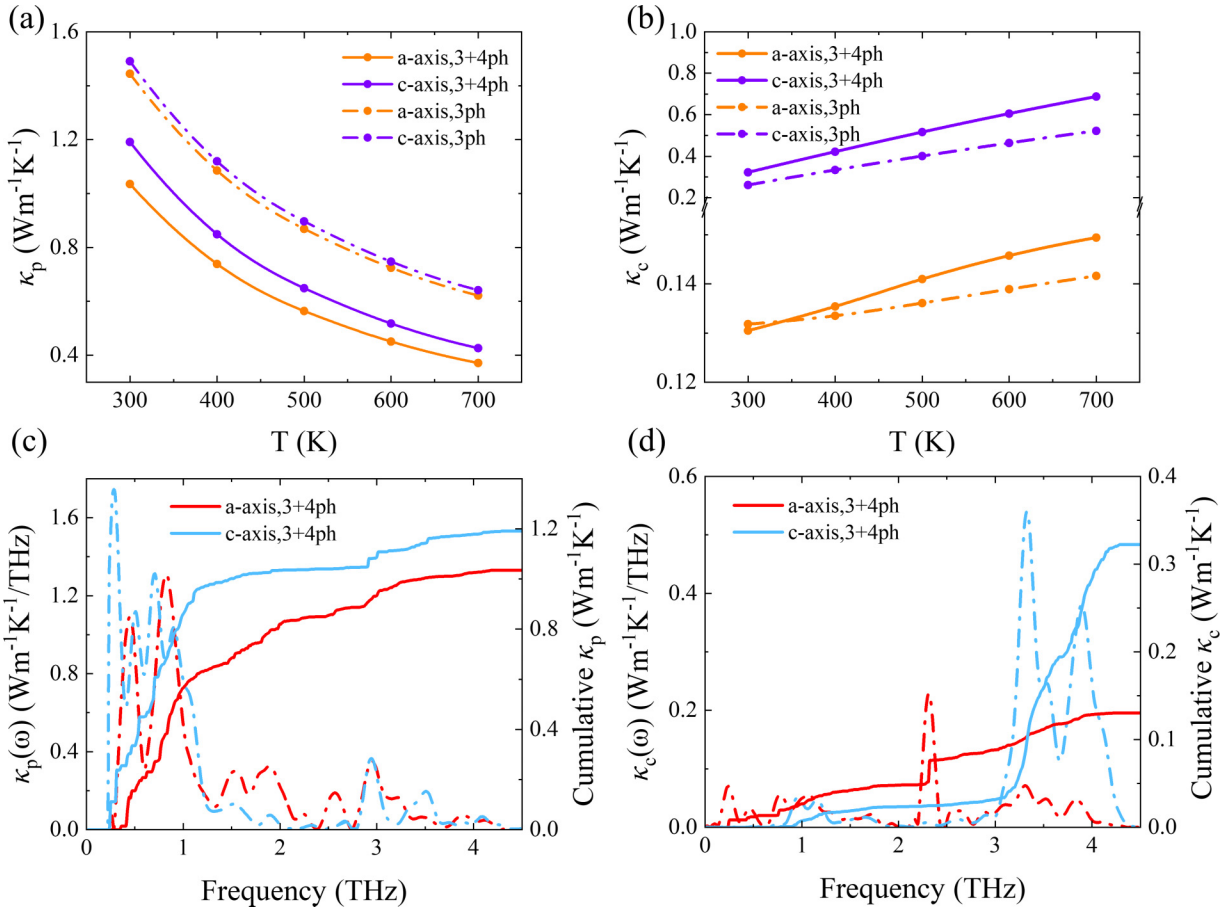

FIG. 3. Plots of (a) κ_p and (b) κ_c in the in-plane (a-axis) and cross-plane (c-axis) directions as a function of temperature for $TlBiSe_2$ considering 3ph and (3 + 4)ph scattering processes. Also plotted are the calculated cumulative (c) κ_p and (d) κ_c along the a and c axes with 3ph and (3 + 4)ph scattering processes versus phonon frequency at 300 K. Solids lines are cumulative κ and dashed lines are differential κ.

culations, the corresponding κ_p is decreased to 1.03 and 1.19 W m^{-1} K^{-1}, respectively. Figures 2(c) and 2(d) show the rate of 3ph and 4ph scattering at 300 and 700 K, respectively. The 4ph scattering rate of acoustic phonons and low-frequency optical phonons is comparable to the 3ph scattering rate at 300 K, which is more obvious at 700 K. The 4ph scattering rate is negligible compared to the 3ph scattering rate at higher frequencies, indicating that the 4ph interaction affects κ_L mainly by increasing the scattering of acoustic phonons. To better differentiate the contribution of acoustic and optical phonons to κ_p, the cumulative and differential κ_p are displayed in Fig. 3(c). It can be observed that acoustic phonons are the main contributors to κ_p, while optical phonons only make a small contribution.

C. Wavelike phonon tunneling effects

In materials with low κ_L, the wavelike phonon tunneling effect is a significant phenomenon that deserves attention [43]. Thus, to gain a better understanding of the thermal transport properties in $TlBiSe_2$, it is necessary to thoroughly investigate the off-diagonal contributions κ_c in κ_L. Similarly, the calculated values of κ_c are also presented in Fig. 3(b). Considering 3ph scattering, the calculated κ_c is 0.13 and 0.26 W m^{-1} K^{-1} at 300 K along the a and c axes, respectively. In the case of (3 + 4)ph scattering, κ_c is 0.13 and 0.32 W m^{-1} K^{-1}, respectively.

In Fig. 4 the orange horizontal line represents the Wigner limit τ_{Wigner} (when the phonon lifetime is equal to the inverse of the average interband spacing [44]), while the red curve represents the Ioffe-Regel limit $\tau_{Ioffe\text{-}Regel}$ (when the phonon lifetime is equal to the inverse of the phonon frequency [44]). Phonons with lifetime $\tau > \tau_{Wigner}$ primarily contribute to κ_p, while those with $\tau_{Ioffe\text{-}Regel} < \tau < \tau_{Wigner}$ mainly govern κ_c. Phonons with $\tau < \tau_{Ioffe\text{-}Regel}$ exhibit overdamping behavior and necessitate the use of spectral-function methodologies for their description [45]. Unlike typical crystals, $TlBiSe_2$ has a significant number of optical phonons with τ between τ_{Wigner} and $\tau_{Ioffe\text{-}Regel}$. The acoustic phonons have larger τ, mainly concentrated in the particlelike region, and also have large group velocities. Therefore, κ_p is primarily dominated by acoustic branches. This also explains that the 4ph interaction reduces κ_L mainly by affecting κ_p as discussed above. After considering 4ph scattering processes, κ_c along the a axis is essentially unchanged and κ_c along the c axis increases slightly. Due to the large τ of 4ph scattering being concentrated in the particlelike region, they have little effect on the wavelike thermal conductivity. It is noteworthy that at 700 K the

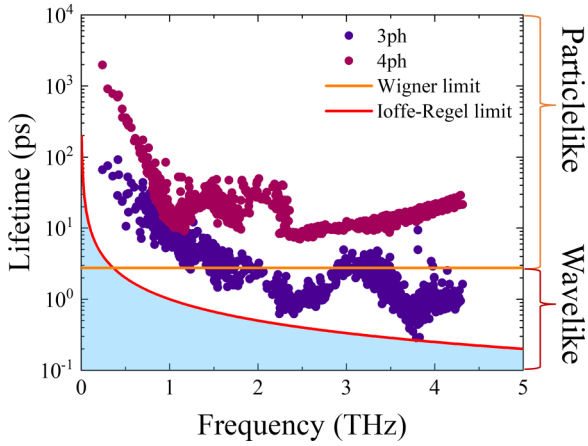

FIG. 4. Comparison of phonon lifetime between 3ph and 4ph scattering at 300 K. The orange solid line is the Wigner limit, which is calculated by $\tau_{\text{Wigner}} = 1/\delta\omega_{\text{av}} = 3N_{\text{at}}/\omega_{\text{max}}$, where ω_{av} is the average interband spacing, N_{at} is the number of phonon branches, and ω_{max} is the maximum phonon frequency. The red solid line is the Ioffe-Regel limit, which is calculated by $\tau_{\text{Ioffe-Regel}} = 1/\omega$.

average value of κ_c is approximately equal to that of κ_p, around 0.4 W m^{-1} K^{-1}.

Figure 3(d) displays the cumulative thermal conductivity of κ_c. It is evident that κ_c is primarily contributed by the optical branches. As previously mentioned, the Tl rattling atoms soften acoustic phonons, making acoustic bunching, which leads to smaller frequency differences in acoustic phonons. From Eq. (3) it can be inferred that acoustic phonons will contribute to the propagation of κ_c. However, in reality, κ_c is mainly contributed by the optical branches. The τ of acoustic phonons are mainly concentrated in the particlelike region, which mostly contributes to κ_p and contributes little to κ_c. The τ of optical phonons is mainly concentrated in the wavelike region, thus contributing to κ_c. This is also why the optical branches serve as the primary contributor to accumulating κ_c. Figure 5 shows the resolved κ_c associated with different phonon pairs along the a axis [Fig. 5(a)] and the c axis [Fig. 5(b)] at 300 K. According to the previous discussion, the optical branches predominantly govern κ_c, which is consistent with the results shown in Fig. 5. The phonon pairs that contribute more to κ_c are mainly distributed on the diagonal in the figure, where ω^s is approximately equal to $\omega^{s'}$. It is worth noting that the phonon pairs in the nondiagonal part also contribute significantly to κ_c in Fig. 5(b). From Eq. (3) it can be seen that the magnitude of the interbranch phonon group velocity also has a significant effect on κ_c. The interbranch phonon group velocity under different phonon pairs is also calculated (see the Supplemental Material [26]). It is clear that the contribution to κ_c in the nondiagonal part is due to the large interbranch phonon group velocity. Figure 6 shows the curves of three different thermal conductivity variations with temperature. The κ_p decreases as the temperature rises, while κ_c exhibits the opposite trend. As depicted in Fig. 6(a), along the a axis, κ_c exhibits minimal changes with increasing temperature, whereas κ_p displays an evident downward trend and the difference between κ_p and κ_c gradually decreases. The κ_L value along the a axis, obtained by the addition of κ_c and κ_p, is close to the experimental results. At high temperatures, κ_c exceeds κ_p and becomes the dominant factor in κ_L along the c axis. As a result, the temperature dependence of κ_L becomes weaker and displays a nonstandard $\kappa_L \propto T^{-0.36}$ dependence along the c axis.

IV. CONCLUSION

We have investigated the effects of the 4ph interactions and wavelike phonon tunneling effects on the thermal transport properties of $TlBiSe_2$. Acoustic phonons are dominated by the vibrations of Tl rattling atoms, which causes the acoustic

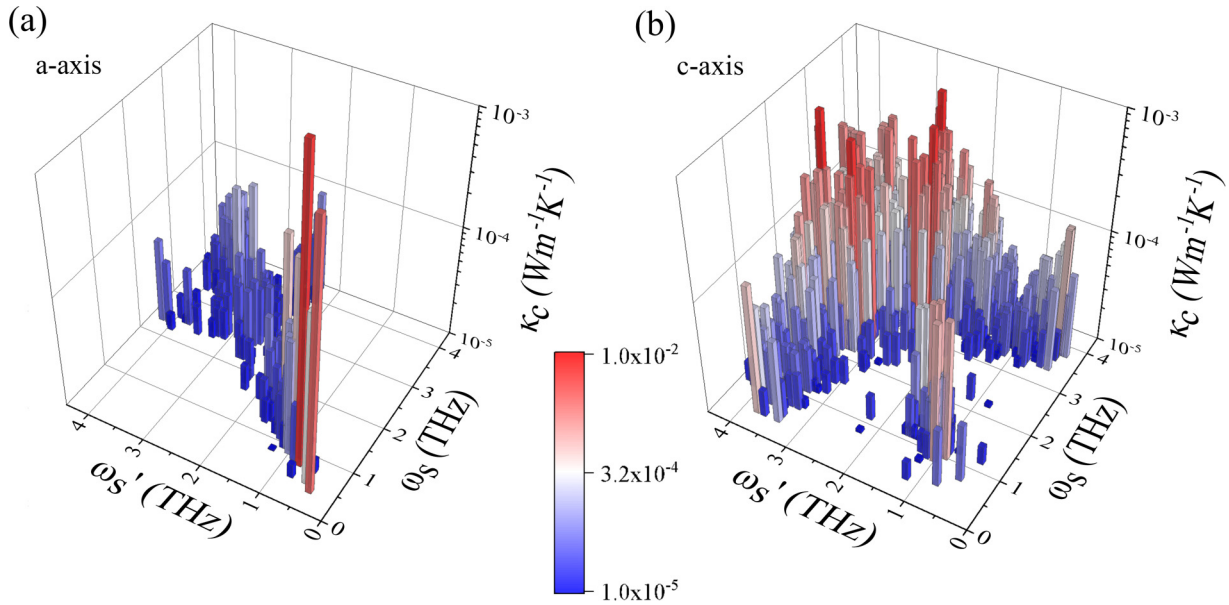

FIG. 5. Three-dimensional stacked bar plots of the off-diagonal terms contributing to κ_L along the a axis and (b) c axis in $TlBiSe_2$ versus the frequency of different phonon pairs.

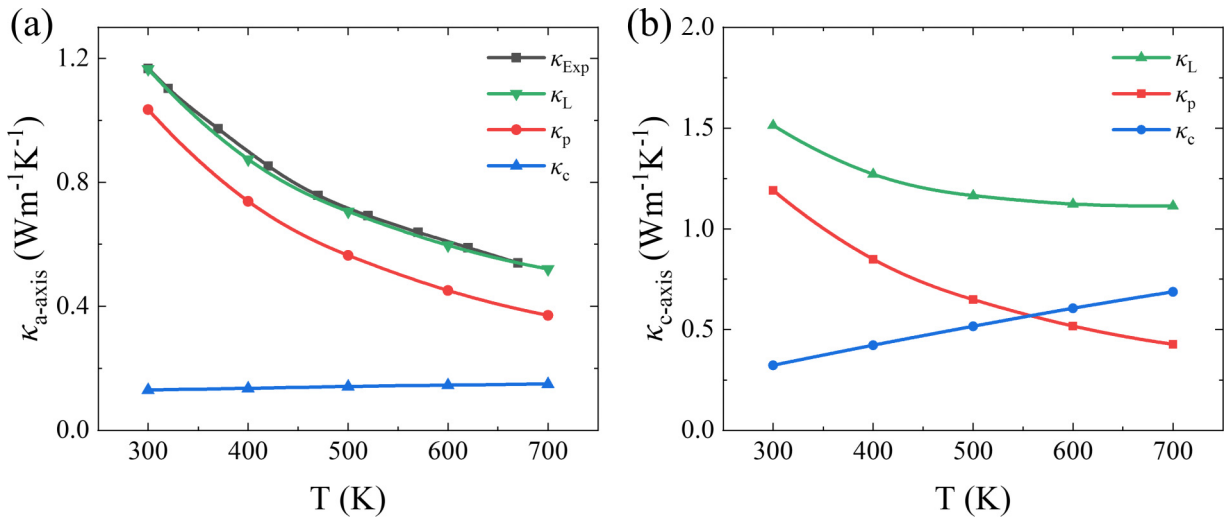

FIG. 6. Lattice thermal conductivity considering (3 + 4)ph scattering processes along (a) the *a* axis and (b) the *c* axis. The red, blue, and green lines represent κ_p, κ_c, and κ_L, respectively. The gray line is the value from experiment [15].

branches to exhibit dense and flat properties. In 3ph scattering processes, scattering channels of *aaa* are severely inhibited and scattering channels of *aoo* are dominant. Considering (3 + 4)ph scattering, the scattering rate of acoustic phonons increases obviously, which has a significant effect on κ_p. At 300 K, after considering 4ph scattering, the κ_p along the *a* axis is reduced by 28% from 1.44 W m^{-1} K^{-1} to 1.03 W m^{-1} K^{-1}. Acoustic phonons have relatively large phonon lifetime τ and are mainly concentrated in the particlelike region. The optical phonons have shorter τ and dominate the wavelike thermal transport. The agreement between the calculated κ_L along the *a* axis and the experimental curve improves with increasing temperature. Along the *c* axis, κ_c will exceed κ_p as the temperature increases and become the main contribution to κ_L, with κ_c contributing 61% to κ_L at 700 K. The large contribution of phonon pairs near the diagonal to κ_c is due to the small frequency difference. The non-negligible contribution of nondiagonal phonon pairs to κ_c is due to the large interbranch phonon group velocity. Our work is of great significance in understanding the thermal transport mechanism in ternary-layered thallium-based semiconductors.

ACKNOWLEDGMENTS

This work was supported by the Natural Science Foundation of China (Grant No. 12304038), Huzhou Natural Science Foundation (Grant No. 2023YZ50), the Startup funds of Outstanding Talents of UESTC (Grant No. A1098531023601205), and National Youth Talents Plan of China (Grant No. G05QNQR049).

[1] G. J. Snyder and E. S. Toberer, Complex thermoelectric materials, Nat. Mater. **7**, 105 (2008).
[2] J. He, M. G. Kanatzidis, and V. P. Dravid, High performance bulk thermoelectrics via a panoscopic approach, Mater. Today **16**, 166 (2013).
[3] Y. Pei, X. Shi, A. LaLonde, H. Wang, L. Chen, and G. J. Snyder, Convergence of electronic bands for high performance bulk thermoelectrics, Nature (London) **473**, 66 (2011).
[4] J. P. Heremans, B. Wiendlocha, and A. M. Chamoire, Resonant levels in bulk thermoelectric semiconductors, Energy Environ. Sci. **5**, 5510 (2012).
[5] L. Müchler, F. Casper, B. Yan, S. Chadov, and C. Felser, Topological insulators and thermoelectric materials, Phys. Status Solidi **7**, 91 (2013).
[6] Y. Xu, Z. Gan, and S.-C. Zhang, Enhanced thermoelectric performance and anomalous Seebeck effects in topological insulators, Phys. Rev. Lett. **112**, 226801 (2014).
[7] L. Müchler, H. Zhang, S. Chadov, B. Yan, F. Casper, J. Kübler, S.-C. Zhang, and C. Felser, Topological insulators from a chemist's perspective, Angew. Chem. Int. Ed. **51**, 7221 (2012).
[8] L. Cheng, H. J. Liu, J. Zhang, J. Wei, J. H. Liang, J. Shi, and X. F. Tang, Effects of van der Waals interactions and quasiparticle corrections on the electronic and transport properties of Bi_2Te_3, Phys. Rev. B **90**, 085118 (2014).
[9] H. Zhang, C.-X. Liu, X.-L. Qi, X. Dai, Z. Fang, and S.-C. Zhang, Topological insulators in Bi_2Se_3, Bi_2Te_3 and Sb_2Te_3 with a single Dirac cone on the surface, Nat. Phys. **5**, 438 (2009).
[10] M. Al-Fahdi, X. Zhang, and M. Hu, Phonon transport anomaly in metavalent bonded materials: Contradictory to the conventional theory, J. Mater. Sci. **56**, 18534 (2021).
[11] B. Singh, A. Sharma, H. Lin, M. Z. Hasan, R. Prasad, and A. Bansil, Topological electronic structure and Weyl semimetal in the $TlBiSe_2$ class of semiconductors, Phys. Rev. B **86**, 115208 (2012).
[12] S. V. Eremeev, Y. M. Koroteev, and E. V. Chulkov, Ternary thallium-based semimetal chalcogenides Tl-V-VI_2 as a new

class of three-dimensional topological insulators, JETP Lett. **91**, 594 (2010).
[13] B. KaniAmuthan, R. Venkatesan, R. Nagaraj, K. Aravinth, and P. Ramasamy, Extolling thermoelectric properties of incommensurate (IC) $TlBiSe_2$ polycrystals prepared by melt temperature oscillation method, Ceram. Int. **49**, 6811 (2023).
[14] G. Ding, J. Carrete, W. Li, G. Y. Gao, and K. Yao, Ultralow lattice thermal conductivity in topological insulator $TlBiSe_2$, Appl. Phys. Lett. **108**, 233902 (2016).
[15] I. Maria, R. Arora, M. Dutta, S. Roychowdhury, U. V. Waghmare, and K. Biswas, Metavalent bonding-mediated dual $6s^2$ lone pair expression leads to intrinsic lattice shearing in n-type $TlBiSe_2$, J. Am. Chem. Soc. **145**, 9292 (2023).
[16] T. Feng, L. Lindsay, and X. Ruan, Four-phonon scattering significantly reduces intrinsic thermal conductivity of solids, Phys. Rev. B **96**, 161201(R) (2017).
[17] X. Yang, T. Feng, J. Li, and X. Ruan, Stronger role of four-phonon scattering than three-phonon scattering in thermal conductivity of III-V semiconductors at room temperature, Phys. Rev. B **100**, 245203 (2019).
[18] Z. Zhang, Y. Guo, M. Bescond, J. Chen, M. Nomura, and S. Volz, Heat conduction theory including phonon coherence, Phys. Rev. Lett. **128**, 015901 (2022).
[19] Y. Wu, Y. Chen, Z. Fang, Y. Ding, Q. Li, K. Xue, H. Shao, H. Zhang, and L. Zhou, Ultralow lattice thermal transport and considerable wave-like phonon tunneling in chalcogenide perovskite $BaZrS_3$, J. Phys. Chem. Lett. **14**, 11465 (2023).
[20] P. Hohenberg and W. Kohn, Inhomogeneous electron gas, Phys. Rev. **136**, B864 (1964).
[21] P. E. Blöchl, Projector augmented-wave method, Phys. Rev. B **50**, 17953 (1994).
[22] J. P. Perdew, K. Burke, and M. Ernzerhof, Generalized gradient approximation made simple, Phys. Rev. Lett. **77**, 3865 (1996).
[23] G. Kresse and J. Furthmüller, Efficiency of *ab-initio* total energy calculations for metals and semiconductors using a plane-wave basis set, Comput. Mater. Sci. **6**, 15 (1996).
[24] R. E. Peierls, *Quantum Theory of Solids* (Oxford University Press, Oxford, 1955).
[25] O. Hellman and I. A. Abrikosov, Temperature-dependent effective third-order interatomic force constants from first principles, Phys. Rev. B **88**, 144301 (2013).
[26] See Supplemental Material at http://link.aps.org/supplemental/10.1103/PhysRevB.109.214307 for details of energy and temperature changes during the 300 and 700 K AIMD simulation, the electronic localization function, phonon spectra with different cutoff radii, calculated phonon group velocities in the irreducible BZ at 300 K, phonon dispersion projected by the Grüneisen parameters at 300 K, and three-dimensional stacked bar plots of the interbranch phonon group velocity versus frequency of different phonon pairs.
[27] W. Li, J. Carrete, N. A. Katcho, and N. Mingo, ShengBTE: A solver of the Boltzmann transport equation for phonons, Comput. Phys. Commun. **185**, 1747 (2014).
[28] Z. Han, X. Yang, W. Li, T. Feng, and X. Ruan, FourPhonon: An extension module to ShengBTE for computing four-phonon scattering rates and thermal conductivity, Comput. Phys. Commun. **270**, 108179 (2022).
[29] Our code is stored at https://github.com/YuWu-thermal/ShengBTE-off-diagonal.
[30] M. Simoncelli, N. Marzari, and F. Mauri, Unified theory of thermal transport in crystals and glasses, Nat. Phys. **15**, 809 (2019).
[31] M. Simoncelli, N. Marzari, and F. Mauri, Wigner formulation of thermal transport in solids, Phys. Rev. X **12**, 041011 (2022).
[32] B. Yan and S.-C. Zhang, Topological materials, Rep. Prog. Phys. **75**, 096501 (2012).
[33] O. Madelung, *Semiconductors: Data Handbook* (Springer Science+Business Media, New York, 2004).
[34] O. Hellman and D. A. Broido, Phonon thermal transport in Bi_2Te_3 from first principles, Phys. Rev. B **90**, 134309 (2014).
[35] M. Christensen, A. B. Abrahamsen, N. B. Christensen, F. Juranyi, N. H. Andersen, K. Lefmann, J. Andreasson, C. R. Bahl, and B. B. Iversen, Avoided crossing of rattler modes in thermoelectric materials, Nat. Mater. **7**, 811 (2008).
[36] J. Li, L. Wei, Z. Ti, L. Ma, Y. Yan, G. Zhang, and P.-F. Liu, Wavelike tunneling of phonons dominates glassy thermal conductivity in crystalline $Cs_3Bi_2I_6Cl_3$, Phys. Rev. B **108**, 224302 (2023).
[37] M. Jian, Z. Feng, Y. Xu, Y. Yan, G. Zhao, and D. J. Singh, Ultralow lattice thermal conductivity induced by anharmonic cation rattling and significant role of intrinsic point defects in $TlBiS_2$, Phys. Rev. B **107**, 245201 (2023).
[38] S. Lee, K. Esfarjani, T. Luo, J. Zhou, Z. Tian, and G. Chen, Resonant bonding leads to low lattice thermal conductivity, Nat. Commun. **5**, 3525 (2014).
[39] L. Lindsay, D. A. Broido, and T. L. Reinecke, First-principles determination of ultrahigh thermal conductivity of boron arsenide: A competitor for diamond? Phys. Rev. Lett. **111**, 025901 (2013).
[40] M. Lax, P. Hu, and V. Narayanamurti, Spontaneous phonon decay selection rule: *N* and *U* processes, Phys. Rev. B **23**, 3095 (1981).
[41] T. Ghosh, M. Dutta, D. Sarkar, and K. Biswas, Insights into low thermal conductivity in inorganic materials for thermoelectrics, J. Am. Chem. Soc. **144**, 10099 (2022).
[42] V. Kurian Elavunkel, S. K. Das, and P. Padhan, Assessing lattice thermal conductivity of topological insulator Bi_2Se_3 by raman thermometry, Phys. Status. Solidi A **221**, 2300792 (2024).
[43] Q. D. Gibson, T. Zhao, L. M. Daniels, H. C. Walker, R. Daou, S. Hébert, M. Zanella, M. S. Dyer, J. B. Claridge, B. Slater *et al.*, Low thermal conductivity in a modular inorganic material with bonding anisotropy and mismatch, Science **373**, 1017 (2021).
[44] Z. Tong, Y. Zhang, A. Pecchia, C. Yam, L. Zhou, T. Dumitrică, and T. Frauenheim, Predicting the lattice thermal conductivity in nitride perovskite $LaWN_3$ from *ab initio* lattice dynamics, Adv. Sci. **10**, 2205934 (2023).
[45] Đ. Dangić, O. Hellman, S. Fahy, and I. Savić, The origin of the lattice thermal conductivity enhancement at the ferroelectric phase transition in GeTe, npj Comput. Mater. **7**, 57 (2021).